Defects induced deep red luminescence of $CaGdAlO_4$-type layered perovskite: multi-cationic sites partial/full substitution and application in pc-LED and plant lighting

Bowen Wang,[a] Changshuai Gong,[a] Xuyan Xue,[a] Meiting Li,[c] Qi Zhu,[d] Xuejiao Wang,[a*] Ji-Guang Li[b*]

[a]College of Chemistry and Materials Engineering, Bohai University, Jinzhou, Liaoning 121007, China
[b]Research Center for Functional Materials, National Institute for Materials Science, Tsukuba, Ibaraki 305-0044, Japan
[c]School of Materials Science and Engineering, Liaoning University of Technology, Jinzhou, Liaoning 121001, China
[d]Key Laboratory for Anisotropy and Texture of Materials (Ministry of Education), School of Materials Science and Engineering, Northeastern University, Shenyang, Liaoning 110819, China.

*Corresponding author

Dr. Xuejiao Wang
Bohai University
Jianzhou, China
Tel: +86-416-3400708
E-mail: wangxuejiao@bhu.edu.cn

Dr. Ji-Guang Li
National Institute for Materials Science
Ibaraki, Japan
Tel: +81-29-860-4394
E-mail: li.jiguang@nims.go.jp

Abstract

A series of $CaGdAlO_4$-type layered perovskite phosphors showing deep red luminescence (λ_{em} = 711 nm, λ_{ex} = 338 nm) were synthesized *via* solid reaction. A comprehensive analysis *via* photoluminescence, X-ray photoelectron spectroscopy, thermoluminescence, and fluorescence decay revealed that the deep red luminescence is related to oxygen defects and particularly oxygen interstitials. The defects related luminescence was effectively regulated through partial substitution of multi-cationic sites (the Ca^{2+} site with Mg^{2+}, Sr^{2+}, Ba^{2+}; the Gd^{3+} site with La^{3+}, Y^{3+}, Lu^{3+}) and full substitution of the Gd^{3+} with Y^{3+}. Remarkably, a 383.3% stronger luminescence was obtained through partial substitution with Lu^{3+}, and the quantum yield of luminescence reached 28.74% which is higher than those of the most previously reported self-luminescence systems. A pc-LED device was fabricated with the phosphor, and the device was showed to have potential application in indoor plant cultivation.

Keywords: Layered perovskite; Defect luminescence; Cationic substitution

1. Introduction

Layered perovskites are a class of compounds derived from perovskite, whose structural formula can be expressed as $ABCO_4$, where A = Sr, Ca, or Ba, B = a rare earth element such as La, Y, or Gd, and C = Al, Sc, Ga, or certain transition metal. These compounds belong to the K_2NiF_4 tetragonal structure type with the space group *I4/mmm*.[1-4] The extensive number of cationic sites and element options for each site make layered perovskite a large family with a wide range of applications. They have the potential for applications in medical detection, plant growth, temperature sensing, solar cells, and optical communication. They have also received considerable research attention in luminescence field mainly as matrix lattices for luminescence of various doped activators, such as $BaLaAlO_4:Eu^{3+}$,[5] $CaGdAlO_4:Mn^{4+}/Mg^{2+}$,[6] $SrLaAlO_4:Tb^{3+}$,[7] $SrLaGaO_4:Mn^{4+}$,[8] and others. We noticed in this work that previous crystal structure analysis for layered perovskites found in $ABCO_4$ the A^{2+}/B^{3+} cations with different valence states occupy the same crystallographic position and are randomly distributed.[9] Thus, disorder-induced traps may be easily formed in $ABCO_4$ compounds since the cations are not in complete order in the local structure. Such a structure may provide defect conditions for self-luminescence. According to previous reports, self-luminescence can be achieved through the inherent defect center including vacancy, gap ion, and anti-sites of the host.[10-12] These defects form defect levels within the band gap of the host material and emit visible light as luminous centers. Traps are decisive factors worth considering for defect luminescence. However, a systematic study of self-luminescence, structural defects, and defect regulation of $ABCO_4$ has rarely been reported. The presence of defects in layered perovskites plays a non-negligible role in many luminescent processes and, therefore,

understanding defects would be helpful in revealing luminescence mechanism and designing phosphors. The materials that emit light through activators are not only expensive but also environmentally unfriendly. Clarifying lattice luminescence plays an essential role in reducing costs, alleviating energy crisis, and reducing environmental pressures.

Rare earth aluminates show advantages of chemical and thermal stability, environmental friendliness, and cheap raw materials. As layered perovskites type aluminates, $CaGdAlO_4$ has the extra merit of low phonon energy (~568 cm^{-1}).[7,13] Benefiting from the crystal structure of layered perovskites and the unique advantages of $CaGdAlO_4$, novel luminescence behavior may be obtained. Moreover, clarifying the defect condition of $CaGdAlO_4$ is also vital for the design and property improvement of $CaGdAlO_4$-based optical materials. Therefore, in this work, a series of self-luminescent layered perovskites $(Ca_{1-x}A_x)(Gd_{1-y}Ln_y)AlO_4$ (A = Mg, Sr, Ba, Ln = La, Y, Lu) were synthesized. The obtained phosphors had a broad excitation band in the 250-450 nm region and exhibited deep red emission at 711 nm. The presence of defects was verified, and the luminescence mechanism was proposed. The luminescence was also regulated through partial/full substitution of multi-cationic sites and adjusting elemental ratios.

2. Experimental Procedure

2.1 Reagents

A series of $(Ca_{1-x}A_x)(Gd_{1-y}Ln_y)AlO_4$ (A = Mg, Sr, Ba; Ln = La, Y, Lu; x = 0, 0.01 and y = 0, 0.01) phosphors were synthesized by a conventional solid-state method with the starting materials of $CaCO_3$ (99.99% pure), MgO (AR pure), SrO (AR pure),

$BaCO_3$ (99% pure), Gd_2O_3 (99.999% pure), La_2O_3 (99.999% pure), Y_2O_3 (99.999% pure), Lu_2O_3 (99.99% pure) and Al_2O_3 (AR pure). The rare earth sources were bought from Huizhou Ruier Rare Chemical Hi-Tech Co. Ltd (Huizhou, China), and the other reagents were purchased from Aladdin Industrial Corporation (Shanghai, China). All the reagents were used without further purification. The reagents were weighed according to the designed compositions, mixed and ground in an agate mortar for 30 min, and then calcined in a furnace at 1500 ℃ for 6 h, with a heating rate of 5 ℃/min below 800 ℃ and 3 ℃/min from 800 to 1500 ℃. After the reaction was completed, the product was cooled to room temperature at 5 ℃/min for characterization. The atmosphere was air for common samples and was changed into N_2 and H_2/N_2 for typical samples to investigate the oxygen defects in the compounds.

2.2 Characterization

Phase identification was performed by X-ray diffractometry (XRD; Model Ultima IV, Rigaku, Tokyo, Japan) operated at 40 kV/40 mA, using nickel filtered Cu-K_α radiation (λ = 0.15406 nm) and a scanning speed of 2 ^{o}/min for 2θ = 5-70^o. The XRD data for Rietveld refinement with the TOPAS software[14] was obtained *via* step-scan, using a step size of 0.01^o and an accumulation time of 5 s. The morphology and elemental distribution of the samples were analyzed by field emission scanning electron microscopy (FE-SEM; Model Tescan MIRA LMS, Tesken). Light absorption and the bandgap energy of the products were studied *via* UV-vis spectroscopy (Model PE-750, PerkinElmer, USA). X-ray photoelectron spectroscopy (XPS) was conducted using a Thermo Scientific K-Alpha analyzer (Thermo Fisher Scientific, Waltham, USA), where the chamber pressure is less than 2.0×10^{-7} Mbar, the spot size is 400 μm, the working voltage is 12 kV, and the filament current is 6 mA. The binding

energies were calibrated by using the C 1*s* line of adventitious carbon as a reference. Photoluminescence properties of the $(Ca_{1-x}A_x)(Gd_{1-y}Ln_y)AlO_4$ phosphors were measured using an FLS 1000 fluorospectrophotometer (Edinburgh Instruments Ltd., Herrsching am Ammersee, Britain) with a 450 W Xe lamp as the excitation source. Fluorescence decay kinetics of the main emissions were measured with the lifetime testing unit of the FLS 1000 equipment. Temperature-dependent luminescence spectra and decay kinetics of the main emissions were measured using the same spectrophotometer, which is equipped with a TAP-02 high temperature controller. Thermoluminescence analysis of the samples was carried out using an SL08 TL dosimeter (Guangzhou Radiation Science and Technology Co. Ltd., Guangzhou, China), with a fixed heating rate of 5 ℃/s in the range of RT-350 ℃.

2.3 Fabrication of LED device

The LED device was fabricated by thoroughly mixing the synthesized phosphor in silicone (Leaftop 9300, Shengzhen Tegu New Materials Co., Ltd, Shenzhen, China), followed by coating the mixture on a 1 w NUV-LED chip (~365 nm emission; San'an Optoelectronics Co., Ltd, Xiamen, China), where the weight ratio of total phosphor powder to silicone is 1:1. The photoelectric properties of the device were measured by a Model OHSP-350M LED Fast-Scan Spectrophotometer (350-1050 nm range, Hangzhou Hopoo Light&Color Technology Co. Ltd., Hangzhou, China).

3. Results and Discussion

3.1 Luminescence properties of $CaGdAlO_4$ and the origin of luminescence

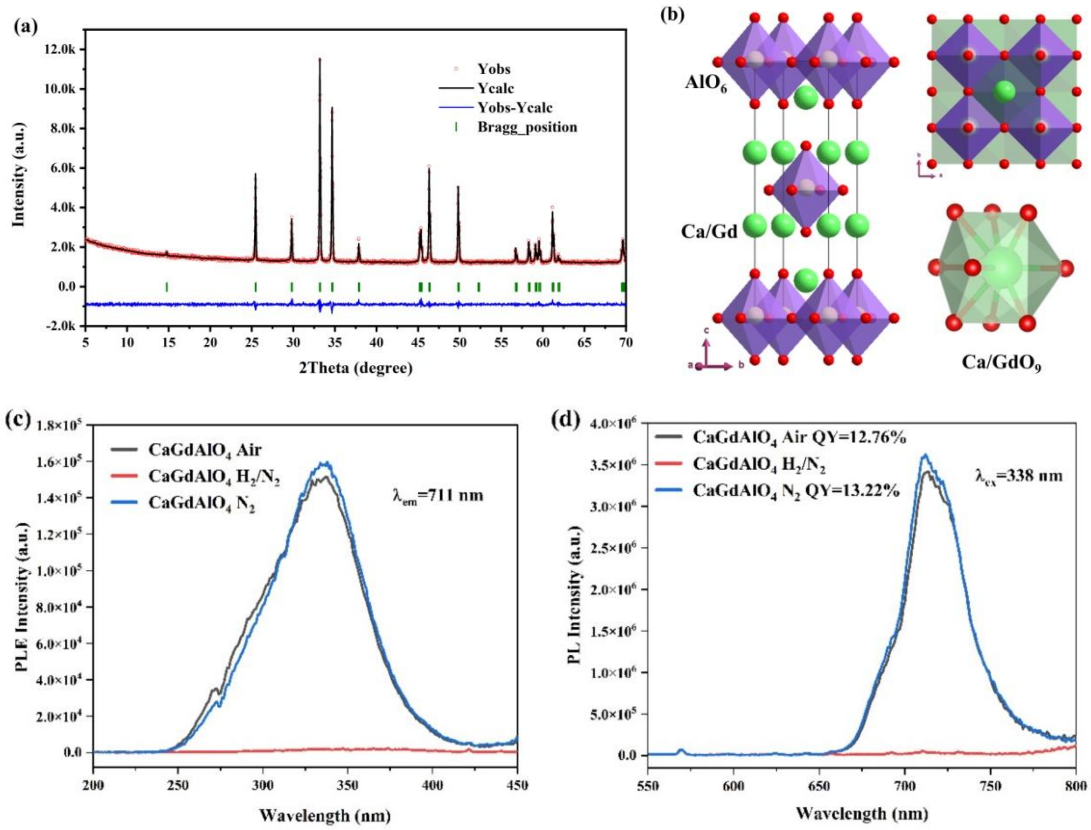

Fig. 1 The Rietveld refinement results, where the observed and calculated patterns, the difference, and the positions of Bragg reflections are in black, red, gray, and green, respectively (a), the crystal structure (b), and the corresponding PLE (c) and PL (d) spectra of $CaGdAlO_4$. The numbers following the compositions in part (d) are the quantum yield (QY) of luminescence.

$CaGdAlO_4$ was synthesized by solid reaction in air, whose XRD pattern and the results of Rietveld refinement are shown in Fig. 1(a). The refinement yielded stable results and acceptable reliability factors as shown in Table 1 and Table 2, which indicate the product is a pure phase. $CaGdAlO_4$ belongs to tetragonal perovskite structure type (*I4/mmm* space group) with lattice constants a = 3.659041(18) Å, b = 3.659041(18) Å and c = 11.98986(12) Å. The $CaGdAlO_4$ compound has a layered crystal structure as shown in Fig. 1(b). In such a structure, Ca/Gd occupy the same site and are 9-fold coordinated by O atoms, with (Ca/Gd)-O bond lengths of ~2.282-2.497 Å, and meanwhile Al is 6-fold coordinated by O to form an octahedron, with a

Al-O bond length of 1.831 Å.

Table 1 Structure parameters and reliability factors obtained *via* refinement of the XRD pattern of $CaGdAlO_4$.

Chemical Formula	$CaGdAlO_4$
Space Group	*I4/mmm*
a (Å)	3.659041(18)
b (Å)	3.659041(18)
c (Å)	11.98986(12)
α (°)	90
β (°)	90
γ (°)	90
V ($Å^3$)	160.5272(20)
R_p	2.30%
R_{wp}	2.96 %
R_{exp}	2.59%
χ^2	1.30

Table 2 Wyckoff positions and atomic coordinates of $CaGdAlO_4$.

Atom	Wyck.	Site	S.O.F.	x/a	y/b	z/c	U[$Å^2$]
Ca1	*4e*	*4mm*	0.5	1/2	1/2	0.14119(12)	0.0024
Gd1	*4e*	*4mm*	0.5	1/2	1/2	0.14119(12)	0.0024
Al1	*2a*	*4/mmm*	-	0	0	0	0.0042
O1	*4c*	*mmm*	-	1/2	1.00000	0	0.0053
O2	*4e*	*4mm*	-	1/2	1/2	0.3330(6)	0.0099

Under the excitation of 338 nm, an emission band centered at 711 nm was observed for $CaGdAlO_4$ (Fig. 1(c) and (d)). Since no activator was added to the host, it was inferred that the observed luminescence is closely related to the defects in the host. The origin of the visible self-luminescence is usually attributed to the presence of various oxygen-related defects including oxygen vacancy (V_o) and interstitial oxygen (O_i) according to previous reports.[15-18] The amount of interstitial oxygen in the crystal of the prepared material would be reduced by annealing in a reducing atmosphere[19] and that of oxygen vacancy would be reduced in an O_2 atmosphere. Thus, $CaGdAlO_4$ powders were synthesized in ambient air, N_2, and a 10 vol% H_2 + 90 vol% gas mixture, respectively, for comparison. Fig. S1 shows the XRD patterns of the samples calcined in different atmospheres. The XRD results showed that the diffraction peaks

are consistent with the standard card. This indicates that the change of atmosphere did not affect the formation of the target product. The corresponding PL and PLE spectra of the three samples are comparatively shown in Fig. 1. As shown in Fig. 1(c), the $CaGdAlO_4$ obtained in air and N_2 has a broadband excitation band centered at 338 nm in the 250-425 nm region. It can be seen from the figure that the spectral features, including peak position and profile of the sample calcined in N_2 have no obvious change compared with the product obtained in air, and the intensity is slightly enhanced. However, the luminescence of the sample calcined in the reducing atmosphere was totally quenched, indicating that the luminescence center disappeared. Since interstitial oxygen is the defect that would be greatly reduced by annealing in H_2/N_2 atmosphere, it can thus be preliminarily determined that the self-luminescence of $CaGdAlO_4$ mainly results from interstitial oxygen defects.

As described in the crystal structure of $CaGdAlO_4$ (Fig. 1(b)), the Ca^{2+}/Gd^{3+} cations with different valence states occupy the same crystallographic position and are randomly distributed. The cations, however, are not in complete order in the local structure,[15] thus disorder-induced traps can be easily formed in $ABCO_4$ compounds as also stated in the study of long afterglow $SrLaAlO_4:Bi^{3+}$ phosphor.[20] In addition, during high-temperature reaction, due to the transfer of oxygen atoms, V_o and O_i come forth simultaneously based on the following reaction:[21]

$$CaGdAlO_4 \rightarrow CaGdAlO_{(4-x)} \cdot xV_O \cdot xO_i \quad (1)$$

O_i becomes dominant and the formation of V_o is restrained during annealing in air because of the absorption of oxygen.

The interstitial oxygen ions are consumed in the reducing atmosphere of $90\%N_2+10\%H_2$, and the reaction may occur as follows:[21]

$$CaGdAlO_{(4-x)} \cdot xV_O \cdot xO_i + H_2 \rightarrow CaGdAlO_{(4-x)} \cdot xV_O + H_2O + xe \quad (2)$$

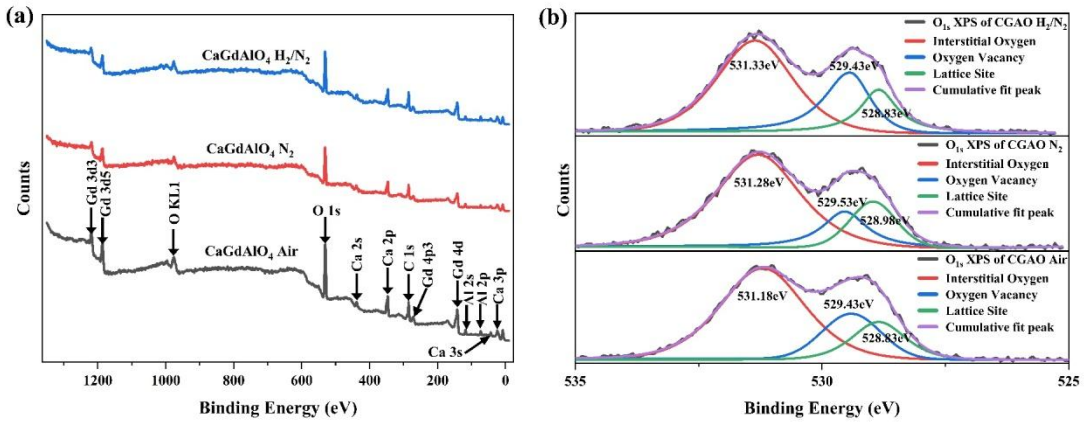

Fig. 2 XPS survey spectra of $CaGdAlO_4$ calcined in different atmospheres (a) and XPS core level scan of O 1*s* (b).

XPS measurement was carried out to investigate the chemical composition and chemical state of O in the products. Fig. 2(a) shows the XPS survey spectra for the $CaGdAlO_4$ calcined in different atmospheres, from which it is obvious that all the spectral features, except for the C 1*s* level, are attributed to the constituent elements of $CaGdAlO_4$. Fig. 2(b) shows the deconvoluted high-resolution XPS spectra of O 1*s* core level, where three distinct Lorentzian–Gaussian peaks centered around binding energies of 528.83, 529.43, 531.33 eV were observed and the peak position is basically invariable for the samples calcined in different atmospheres. According to previous reports, the O 1*s* state always contains three binding energy components, which are low binding energy peak (LP), middle binding energy peak (MP), and high binding energy peak (HP) centered at ~530.23 eV (LP), 531.57 eV (MP), and 532.60 eV (HP).[22-24] The LP, MP, and HP are attributed to lattice site oxygen (O_L), oxygen vacancy (V_o), and interstitial oxygen (O_i), respectively.[23,24]

The change of oxygen defects can be roughly estimated by the intensity ratio of the MP (V_o) and HP (O_i) peaks corresponding to the fitting results. The intensity ratios in strength and area for MP (V_o), and HP (O_i) are summarized in Table S1. It can be seen that, compared with the sample calcined in air, the O_i:V_o intensity ratio

decreased for the sample prepared in the reducing atmosphere. This indicates a decreased content of O_i, and corresponds well with the observed luminescence quenching of the sample annealed in reducing atmosphere. Furthermore, the O_i:V_o intensity ratio and the observed emission intensity (Fig. 1) shared the same trend. The increased O_i:V_o intensity ratio by annealing in N_2 proved that O_i was not solely provided by O_2 absorption from air (O_i = 1/2O_2).

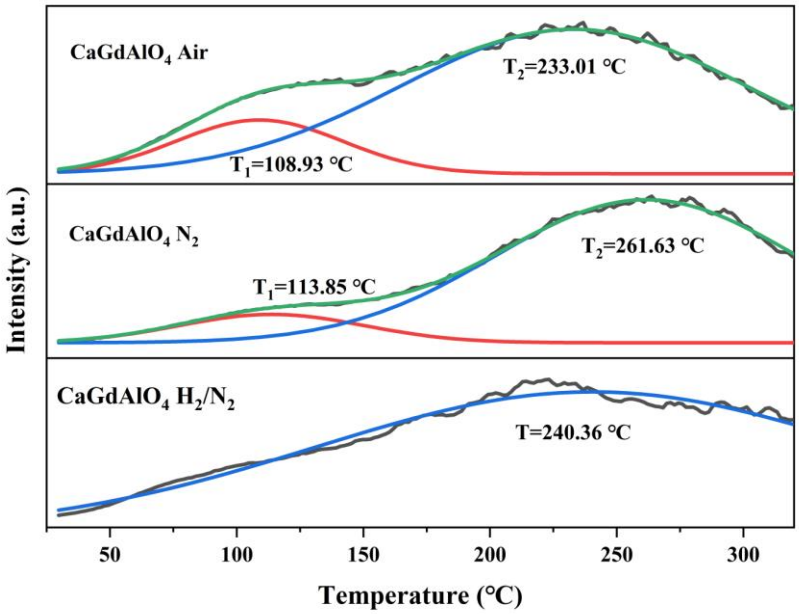

Fig. 3 Thermoluminescence analysis for the $CaGdAlO_4$ powders calcined in different atmospheres.

Fig. 3 shows the thermoluminescence spectra (TL) of the samples calcined in different atmospheres. The results of spectral fitting showed that two sub-peaks are responsible for the TL of the samples calcined in N_2 and in air, which indicates the existence of two defect levels. The depths of electron traps can be estimated with the following equation:[25]

$$E = \frac{T_m}{500} \tag{3}$$

where T_m is the peak temperature (in Kelvin) of the sub-peak. The depths of the two electron traps can therefore be calculated to be $E_{Trap1} \approx 0.8$ eV (shallow defect) and

E_{Trap2} ≈ 1.0 eV (deep defect) as shown in Table S2. However, the absence of sub-peak 1 for the product calcined in H_2 implies that this electron trap may be the main origin of the observed luminescence. According to the above analysis and the totally quenched luminescence by calcination in H_2/N_2 atmosphere (Fig. 1), the shallow and deep defects are inferred to be interstitial oxygen and oxygen vacancy, respectively.

Trap density (N_0) can be estimated from the following equation:[25]

$$N_0 = \frac{\omega \times I_m}{\beta \times [2.52 + 10.2 \times (\mu_g - 0.42)]} \quad (4)$$

where I_m is the intensity of the TL peak, β is the heating rate, ω is the FWHM defined as τ + δ, while τ and δ are the half-width at low and high temperatures, respectively, μ_g is the asymmetry parameter defined as δ/(τ + δ). The trap densities of the products calcined in different atmospheres are shown in Table S2. It can be seen that N_{01} (the trap density for trap 1) increased by annealing in N_2, in compliance with the observed luminescence increment.

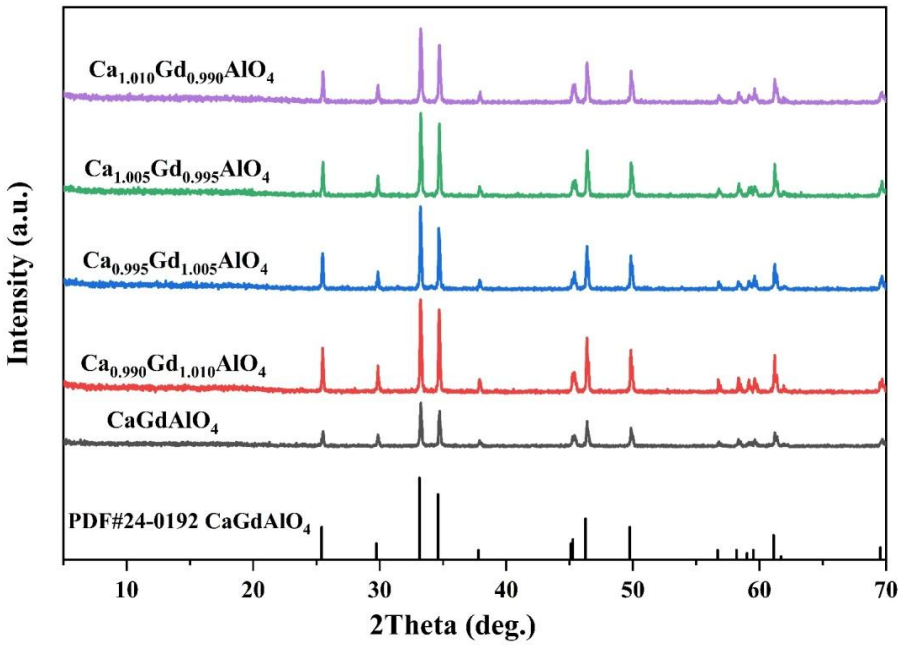

Fig. 4 XRD patterns of the products with tuned Ca:Gd atomic ratios.

Solid reaction in the air produced $CaGdAlO_4$ products with varying Ca:Gd atomic

ratios, whose XRD patterns are shown in Fig. 4. It can be seen from the XRD patterns that all the samples including the nonstoichiometric ones are pure phases and can be well indexed to the $CaGdAlO_4$ standard (PDF # 24-0192).

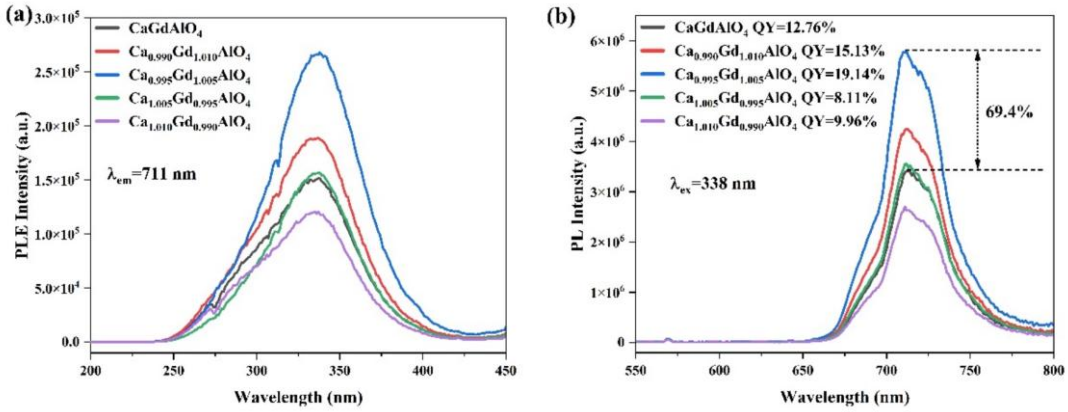

Fig. 5 PLE (a) and PL (b) spectra of the $CaGdAlO_4$ samples with varying Ca:Gd ratios. The numbers following the compositions in part (b) are the quantum yields of luminescence.

The luminescence behaviors of products obtained by adjusting the Ca:Gd ratio (Ca:Gd<1 and Ca:Gd>1) are shown in Fig. 5. It is worth noting that luminescence intensity increases when Gd is excessive (Ca:Gd<1) and decreases when Ca is excessive (Ca:Gd>1). Specifically, a 69.4% enhancement was observed for the Gd excessive sample of $(Ca_{0.995}Gd_{1.005})AlO_4$ and a 21.0% decrease was found for the Ca excessive sample of $(Ca_{1.010}Gd_{0.990})AlO_4$, when compared with the stoichiometric composition of $CaGdAlO_4$. The phenomena provided strong evidence for the above conclusion that O_i is responsible for the observed luminescence since excessive Gd^{3+} would produce more O_i and excessive Ca^{2+} on the other hand would introduce extra V_o.

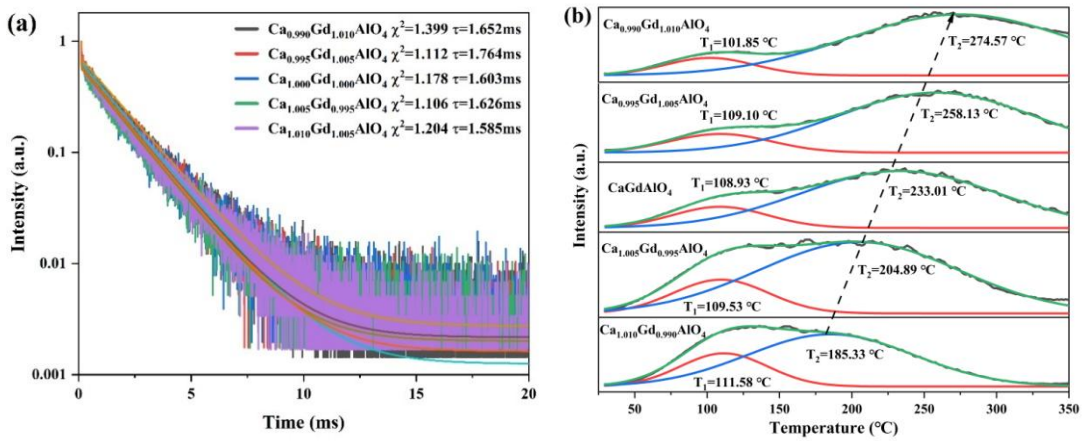

Fig. 6 Decay analysis of the main emission (a) and thermoluminescence analysis (b) for the $CaGdAlO_4$ samples with different Ca:Gd ratios.

The fluorescence decay curves of the series of samples with different Ca:Gd ratio are shown in Fig. 6(a), and it was found that the curves can be well fitted with the following double exponential function:[26]

$$I = A_1 \exp\left(-\frac{t}{\tau_1}\right) + A_2 \exp\left(-\frac{t}{\tau_2}\right) \quad (5)$$

where the I is the luminescence intensity at time t, A_1 and A_2 the constants, and τ_1 and τ_2 are the decay times of the two exponential components. The average lifetime τ can then be determined with the equation:[27]

$$\tau = \left(A_1\tau_1^2 + A_2\tau_2^2\right)/(A_1\tau_1 + A_2\tau_2) \quad (6)$$

The double exponential decay indicates that two kinds of electronic defects exist in the samples. The detailed fitting results can be found in Table S3. The $(Ca_{0.995}Gd_{1.005})AlO_4$ sample has a longer average lifetime of 1.764 ms, which may indicate that there are more defects and corresponds with the fact that this sample has the strongest luminescence. The results once again prove that the non-stoichiometric design with excessive Gd^{3+} created more O_i defects inside the crystal and hence produced stronger luminescence with a longer lifetime.

Fig. 6(b) shows thermoluminescence spectra (TL) and the results of spectral fitting for the series of samples with varying Ca:Gd ratio. The TL spectra showed that two

sub-peaks are responsible for luminescence, which correspond to interstitial oxygen and oxygen vacancy defects. The depths of the two traps and the densities of the defects were derived with the aforementioned equations, and the results are summarized in Table S4. It can be found that the $(Ca_{0.995}Gd_{1.005})AlO_4$ sample has the highest trap densities. Interestingly, it was noted that as the content of Ca decreased, the thermoluminescence shifts to a higher temperature. This is due to the fact that a lower Ca content would reduce oxygen vacancy according to $2Ca^{2+} \xrightarrow{2Gd^{3+}} 2Ca_{Gd}^{'} + V_o^{\cdot\cdot}$. As the concentration of $V_o^{\cdot\cdot}$ decreases, electron and $V_o^{\cdot\cdot}$ would have fewer probability for recombination. As a result, the electron and $V_o^{\cdot\cdot}$ charge pair is eliminated slower and the thermoluminescence maximum is reached at a higher temperature.[28,29]

Fig. S2(a) shows the UV-vis absorption spectrum of $CaGdAlO_4$, where it is seen that the compound mostly absorbs UV light of 250-310 nm. The sharp peak at 275 nm was ascribed to the $^8S_{7/2} \rightarrow {}^6I_J$ excitation transition of Gd^{3+} ions.[27,30-31] Estimation of bandgap energy can be made from the absorption spectrum with Tauc's formula:[32]

$$(\alpha h\nu)^{1/n} = K(h\nu - E_g) \quad (7)$$

where $n = 2$ for an indirect semiconductor and K, α, and $h\nu$ are a constant, absorbance, and photon energy, respectively. From the $(Ah\nu)^{1/2}$ versus $h\nu$ plot, where A is a constant proportional to α, the bandgap energy of $CaGdAlO_4$ was assayed to be ~2.54 eV by extrapolating the linear part of the curve. The bandgap value determined in this work complies well with the 2.45 eV provided on the materials project website.

It is well known that substrates with self-luminescence usually emit blue light under 254 nm excitation due to oxygen deficiency.[33-35] In this study, 711 nm deep red emission was generated using 338 nm excitation, benefiting from the bandgap feature of the studied compounds. The mechanism of luminescence was proposed based on the above analysis and is schematically illustrated in Fig. S2(b). The bandwidth of

$CaGdAlO_4$ is 2.54 eV and a shallow (~0.8 eV) and a deep (~1.0 eV) defect level exist below the conduction band. Under UV excitation, the electrons are promoted to the conduction band, followed by transition to the shallow trap through a non-radiative process, and some electrons are stored in the deep trap. The electrons at the shallow trap return to the valence band and combine with the holes, releasing energy to produce the deep-red emission at 711 nm.

3.2 Partial substitution of multi cationic sites for luminescence engineering of $CaGdAlO_4$

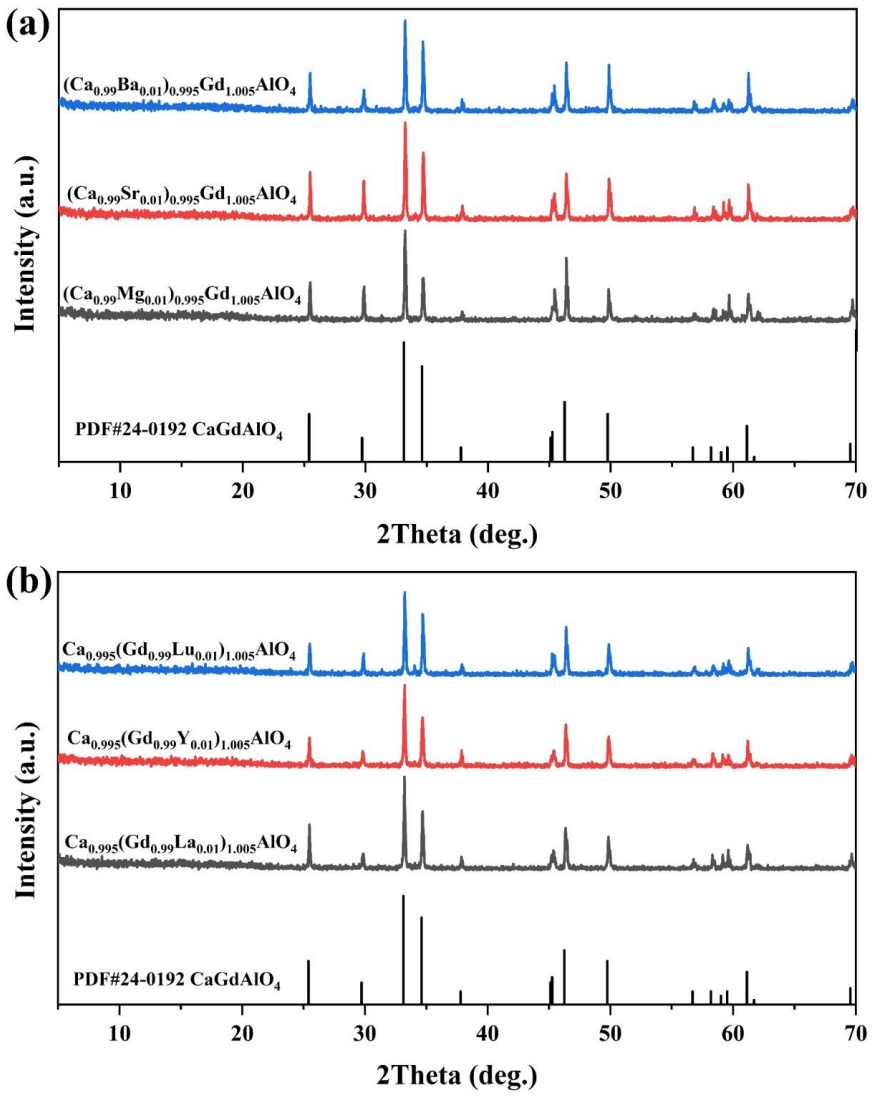

Fig. 7 The XRD patterns of products whose Ca site (a) and Gd site (b) were partially substituted.

Through varying Ca:Gd ratio, it was identified that $(Ca_{0.995}Gd_{1.005})AlO_4$ has the strongest luminescence. This composition was thus selected for partial substitution investigations. Fig. 7 shows the XRD patterns of the Ca-site and Gd-site partially substituted $(Ca_{0.995}Gd_{1.005})AlO_4$ products, where it was found all the diffractions of each product agreed with those of the $CaGdAlO_4$ standard. To check chemical composition, we performed elemental mapping for the samples substituted with Mg^{2+} and Lu^{3+}, as shown in Fig. S3. It is clear that the different cations Ca, Gd, Al, Mg and Lu are uniformly dispersed throughout the entire particle.

The relative difference in ionic radius (D_r) can be calculated *via* the following equation:[36]

$$D_r = \frac{R_m(CN) - R_d(CN)}{R_m(CN)} \times 100\% \quad (8)$$

where R_m and R_d represent the effective radii of the host cation and the dopants, respectively. The ion radii of the involves cations and their D_r relative to Gd^{3+} are summarized in Table S5.

Fig. S4 shows the UV-vis absorption spectra of the Ca- and Gd-site partially substituted products. It can be found that the $^8S_{7/2} \rightarrow {}^6I_J$ excitation transition of Gd^{3+} ions appeared at 275 nm for all the samples. The substitution of either the Ca- or Gd-site did not change the profile of the spectra, but the samples substituted by Mg^{2+} and Lu^{3+} showed the strongest absorption. This corresponds well with the fact that these two samples have the strongest luminescence, as shown later. Besides, the observed absorption intensity varies following the sequence of luminescence intensity for the series of samples.

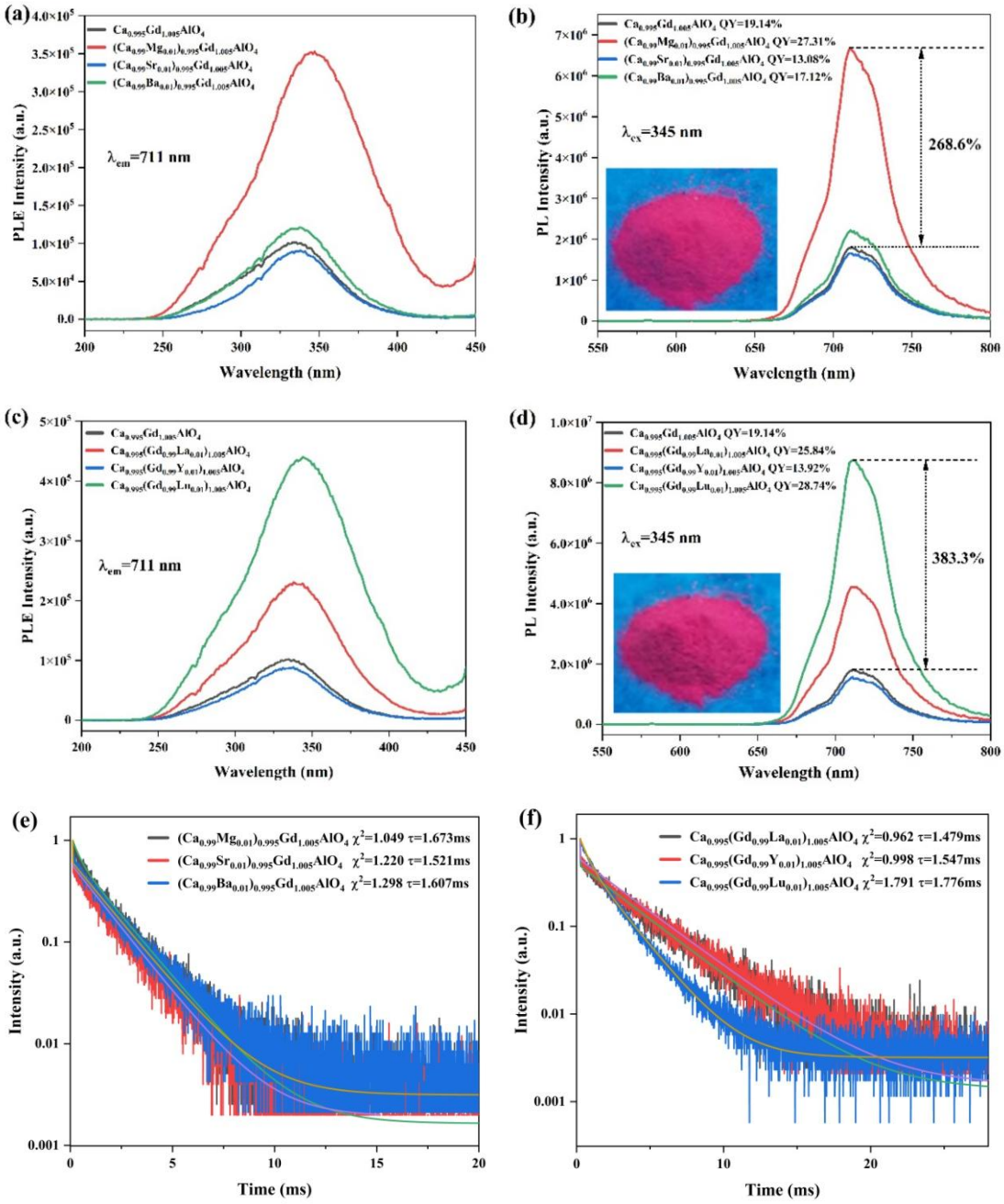

Fig. 8 PLE (a, c) and PL (b, d) spectra of the Ca-site (a, b) and Gd-site (c, d) partially substituted products. The numbers following the compositions in the PL spectra are the quantum yields of luminescence. Parts (e) and (f) are the decay curves for the main emissions of the corresponding products.

The luminescence spectra of the products whose Ca-site and Gd-site were partially substituted by M^{2+} (M = Mg, Sr, Ba) and RE^{3+} (RE = La, Y, Lu), respectively, are shown in Fig. 8. The results showed that the spectral features of luminescence are unchanged by the substitution, when compared with that of the $(Ca_{0.995}Gd_{1.005})AlO_4$ composition. It can be seen that except for Y^{3+} and Sr^{2+} substitution, the luminescence

intensity of the samples substituted by Mg^{2+}, Ba^{2+}, La^{3+} and Lu^{3+} all increased. The products substituted by Mg^{2+} and Lu^{3+} showed the strongest luminescence across the series, whose emission intensity enhanced 268.6% and 383.3% of that of $(Ca_{0.995}Gd_{1.005})AlO_4$.

The greatly enhanced luminescence by partial substitution with Mg^{2+} and Lu^{3+} may have two reasons. One is significant enhancement of UV absorption, including the 345 nm excitation light, as shown in Fig. S4, and the other one should be higher concentrations of O_i defects. It is clear in this work that the intensity of luminescence is closely related to the content of O_i defects, while the formation of such defects is significantly influenced by lattice distortion/stretching.[37] After the partial substitution of the Ca/Gd sites, the distortion inside the crystal is enhanced and the stretching deformation becomes larger, which in turn increases the concentration of O_i and finally the intensity of luminescence. It can be found in Table S5 that Mg^{2+} and Lu^{3+} have the largest and second largest size differences relative to Ca^{2+} and Gd^{3+} (D_r = -24.6% for Ca-Mg, and D_r = -6.8% for Gd-Lu) and, therefore, the strongest luminescence was observed. As the Y^{3+} and Sr^{2+} dopants have small size differences with Gd^{3+} and Ca^{2+} (D_r = 9.9% for Ca-Sr, and D_r = -2.9% for Gd-Y), the induced lattice distortion is limited and the UV absorption after Y^{3+} and Sr^{2+} substitution is decreased, and hence a decreased luminescence was observed.

At the same time, the quantum efficiency reached the maximum values of 27.31% and 28.74% after the partial substitution by Mg^{2+} and Lu^{3+}, respectively (Fig. S5). Quantum efficiency is an important parameter to evaluate the optical properties of phosphors, and the values obtained in this work are higher than those of most previously reported self-activated phosphors, such as $Sr_3LiSbO_6:Gd^{3+}$ (25.2%),[38] $Ca_5Zn_4(VO_4)_6$ (15.9%),[39] $Ca_2NaZn_2V_3O_{12}$ (17.4%),[40] and ZnO (20%).[41] The Quantum efficiency is also higher than the values obtained for typical rare earth activators of Eu^{3+} and Tb^{3+} in $CaGdAlO_4$, as shown in Fig. S6.

The main emissions of the Ca and Gd sites partially substituted products also decayed in a bi-exponential behavior, and the detailed fitting results are shown in Table S6. The products partially substituted by Mg^{2+} and Lu^{3+} showed slightly longer average lifetimes of 1.673 ms and 1.776 ms, respectively. Especially, the τ_1 component became 95 and 158 times longer after Mg^{2+} and Lu^{3+} substitution, respectively. This may indicate that τ_1 corresponds to luminescence from the shallow defects. This also complies well with the fact that the two samples have the strongest luminescence among the series and the sample substituted by Lu^{3+} is better luminescent than that substituted with Mg^{2+} (Fig. S7).

3.3 Full substitution of the Gd-site for luminescence engineering of $CaGdAlO_4$

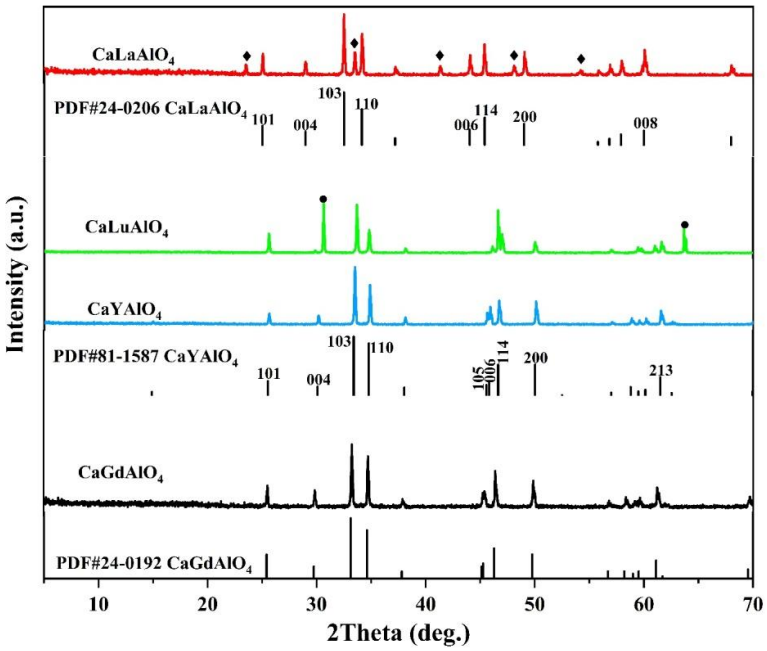

Fig. 9 XRD patterns of the products whose Gd-site was fully substituted by La^{3+}, Y^{3+} and Lu^{3+}.

Fig. 9 shows the XRD patterns of the products whose Gd site was fully substituted by La, Y, Lu, respectively. It was found that the one substituted with Y matches exactly with the $CaYAlO_4$ standard (PDF#81-1587) and does not contain any impurity. Compared with the $CaLaAlO_4$ standard (PDF#24-0206), however, the product substituted by La has some impurities as labeled with black squares. The one

substituted with Lu was compared with $CaYAlO_4$, since the standard diffraction file of $CaLuAlO_4$ is unavailable,[42] and it was found that the product is a phase mixture (impurity marked with black circles). The appearance impurities upon full substitution by La^{3+} and Lu^{3+} is due to the large size difference (D_r) relative to Gd^{3+}, which is 8.9% for La^{3+}-Gd^{3+} and -6.8% for Lu^{3+}-Gd^{3+} (-2.9% for Y^{3+}-Gd^{3+}).

The UV-vis absorption spectra of $CaGdAlO_4$ and $CaYAlO_4$ are shown in Fig. S8(a), where it is seen that the $^8S_{7/2} \rightarrow {}^6I_J$ transition of Gd^{3+} appeared at 275 nm in $CaGdAlO_4$ and is absent in $CaYAlO_4$. Y substitution for Gd significantly enhanced the UV absorption, which well corresponds with the fact that $CaYAlO_4$ has a better luminescence.

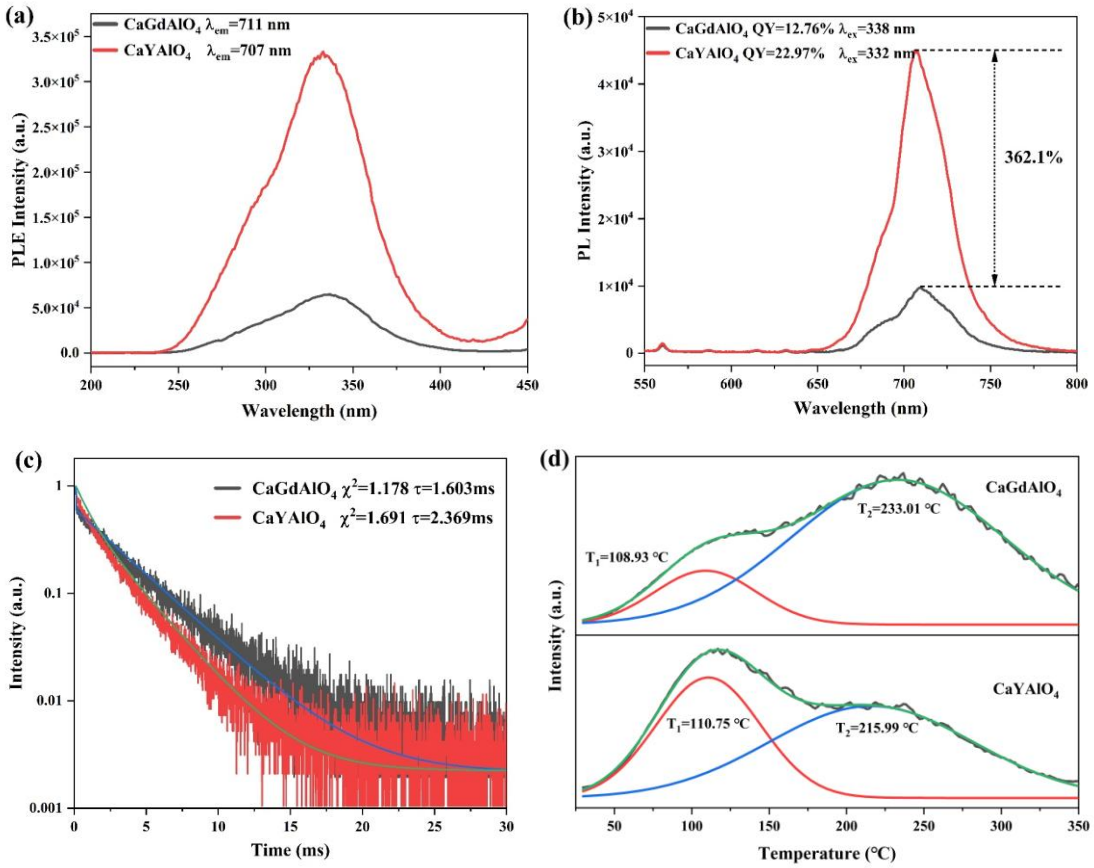

Fig. 10 PLE (a) and PL (b) spectra, decay kinetics of the main emission (c), and fitting of the thermoluminescence curves (d) for $CaYAlO_4$ and $CaGdAlO_4$. The numbers following the compositions in the PL spectra are the quantum yields of the corresponding products.

Since $CaLaAlO_4$ and $CaLuAlO_4$ were not synthesized as pure phase, only the

luminescence of $CaYAlO_4$ and $CaGdAlO_4$ was compared in Fig. 10(a) and (b). It can be seen from the figure that, compared with $CaGdAlO_4$, the emission position of $CaYAlO_4$ did not appreciably change, but the intensity of emission was greatly improved (362.1% enhancement) and the quantum efficiency of luminescence was substantially increased to ~23%. This can also be explained from the much stronger UV absorption of $CaYAlO_4$. Besides, substitution of Gd^{3+} with smaller Y^{3+} (Table S5) may increase the content of O_i defects, which also enhances luminescence.

Fig. 10(c) shows the fluorescence decay curves of the above two samples, and $CaYAlO_4$ was analyzed to have an obviously longer average lifetime τ_{av}. The τ_1 of $CaYAlO_4$ is 257 times longer than that of $CaGdAlO_4$, and the τ_2 of $CaYAlO_4$ is slightly longer (1.58 times) than that of $CaGdAlO_4$ (Table S7). This corresponds well with the above analysis and indicates that τ_1 corresponds to the luminescence from the shallow defect levels. The thermoluminescence spectra and the results of fitting are shown in Fig. 10(d) and Table S8. It can be seen that $CaYAlO_4$ has an obviously stronger sub-peak 1 than $CaGdAlO_4$, indicating a higher concentration of shallow defects. The N_{01} is 3.2 times larger while the N_{02} is slightly lower than the values of $CaGdAlO_4$, which further proves that the observed luminescence is largely from shallow defects.

3.4 Application of the deep red phosphor in plant lighting

Fig. 11(a) shows the electroluminescence (EL) spectra of the pc-LED device fabricated by the $Ca_{0.995}(Gd_{0.99}Lu_{0.01})_{1.005}AlO_4$ phosphor under different operating currents, where the insets show the appearances of the device with current on and off in natural light and with 590 nm filter. It can be seen that the luminescence gradually gains intensity with increasing current. Fig. 11(b) compares the EL spectrum of the pc-LED device (driving current: 20 mA) and the absorption spectrum of phytochrome

P_{FR}.[38,43] As inferred from the significant spectral overlapping, the device may find potential application in indoor plant lighting.

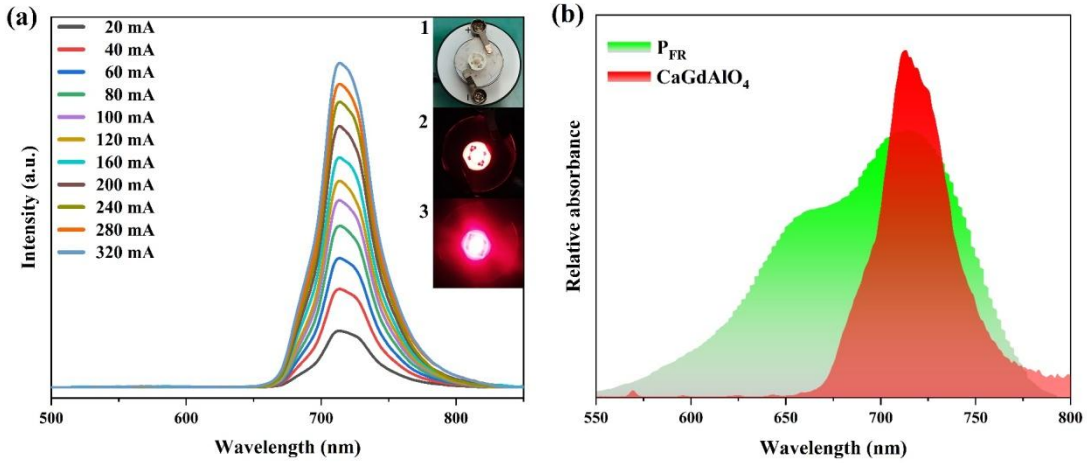

Fig. 11 The electroluminescence spectra of the pc-LED device fabricated by using the $Ca_{0.995}(Gd_{0.99}Lu_{0.01})_{1.005}AlO_4$ phosphor and a 365 nm near-UV chip under different driving currents (a), and comparison of the electroluminescence spectrum of the pc-LED device with the absorption band of phytochrome P_{FR} (b). The insets in (a) show the pictures of the fabricated pc-LED device with current on (20 mA) and off in natural light (1-2) and with 590 nm filter (3).

Conclusions

A series of $CaGdAlO_4$-type layered perovskites were obtained through solid-state reaction, whose luminescence was effectively regulated *via* partial and full substitution of multi cationic sites. The origin of luminescence was comprehensively investigated, and the main conclusions are as follows:

(1) $CaGdAlO_4$ exhibited deep red luminescence at 711 nm under 338 nm excitation, and the self-luminescence was analyzed to mostly originate from oxygen interstitials (O_i).

(2) By partially substituting the Ca and Gd sites with Mg^{2+}/Ba^{2+} and Lu^{3+}/La^{3+}, respectively, the luminescence of $CaGdAlO_4$ was effectively enhanced, which is due to increased UV absorption and a higher O_i concentration by lattice distortion. Remarkably, substitution with Lu^{3+} led to a 383.3% enhancement in luminescence, and the quantum yield reached 28.74%, which is higher than those of most previously

reported self-luminescent materials.

(3) Phase pure compound can be obtained by fully substituting the Gd site with Y, and impurity phase appeared when Gd is fully replaced by either La or Lu owing to large size mismatch. $CaYAlO_4$ exhibited a 362.1% stronger luminescence than $CaGdAlO_4$.

(4) The pc-LED device fabricated from the $Ca_{0.995}(Gd_{0.99}Lu_{0.01})_{1.005}AlO_4$ phosphor and a 365 nm LED chip showed potential application in plant lighting due to a high degree of spectral overlapping between the electroluminescence spectrum of the pc-LED and the P_{FR} photosensitive pigment of the plant.

Author contributions

All the authors have contributed to this research and agreed to submit this work for publication.

Conflicts of interest

There are no conflicts to declare.

Acknowledgements

This work is supported by the Natural Science Foundation of Liaoning Province (Grant No. 2020-MS-286). The authors would like to thank Jian-ming Liu from Shiyanjia Lab (www.shiyanjia.com) for the XPS analysis.

References

1 W. Hasni, A. Boukortt, B. Bekkouche, S. Kacimi, M. Djermouni and A. Zaoui, *Phys. B*, 2012, **407**, 901-906.

2 T. He, Q. Huang, A. P. Ramirez, Y. Wang, K. A. Regan, N. Rogado, M. A. Hayward, M. K. Haas, J. S. Slusky, K. Inumara, H. W. Zandbergen, N. P. Ong and R. J. Cava, *Nature*, 2001, **411**, 54-56.

3 E. Bousquet, M. Dawber, N. Stucki, C. Lichtensteiger, P. Hermet, S. Gariglio and P. Ghosez, *Nature*, 2008, **452**, 732-736.

4 R. Terki, H. Feraoun, G. Bertrand and H. Aourag, *Phys. Status Solidi B*, 2005, **242**, 1054-1062.

5 A. Azhagiri, V. Ponnusamy and R. S. Kumar, *Opt. Mater.*, 2019, **90**, 127-138.

6 J. X. Hu, T. H. Huang, Y. P. Zhang, B. Lu, H. Q. Ye, B. J. Chen, H. P. Xia and C. Y. Ji, *Dalton Trans.*, 2019, **48**, 2455-2466.

7 S. Devi, A. Khatkar, V. B. Taxak, A. Hooda, P. Sehrawat, S. Singh and S. P. Khatkar, *J. Lumin.*, 2020, **221**, 117064.

8 C. Y. Jiang, X. Zhang, J. Wang, Q. Z. Zhao, K.-L. Wong and M. Y. Peng, *J. Am. Ceram. Soc.*, 2019, **102,** 1269-1276.

9 Z. H. Xing, P. L. Li, D. J. Dai, X. T. Li, C. J. Liu, L. Zhang and Z. J. Wang, *Inorg. Chem.*, 2019, **58**, 4869-4879.

10 Z. P. Wang, Z. J. Wang, J. J. Liu, Y. B. Li, X. Y. Meng, K. L. Qiu, Q. Bao, Y. Chen, Z. P. Yang and P. L. Li, *J. Lumin.*, 2019, **207**, 602-612.

11 Z. Y. Yang, S. Q. Lai and Z. G. Xia, *J. Solid State Chem.*, 2020, **288**, 121408.

12 B. Ma, J. Y. Ding, Q. Long and Y. H. Wang, *J. Lumin.*, 2019, **208**, 388-393.

13 N. Zhang, H. Y. Wang, Y. Q. Yin, T. Wang, Z. T. Jia, J. Zhang, Q. Q. Hu, N. Lin, X. W. Fua and X. T. Tao, *CrystEngComm*, 2020, **22**, 955-960.

14 *Bruker AXS TOPAS V4: General profile and structure analysis software for powder diffraction data. - User's Manual*, Bruker AXS, Karlsruhe, Germany, (2008).

15 M. A. Subramanian and A. W. Sleight, *Solid State Sci.*, 2002, **4**, 347-351.

16 J. X. Zhao, S. C. Han, Y. N. Ding, X. Li, A. W. Tang, N. Fu, Z. Y. Liu, F. H. Wang, G. Y. Dong and L. Guan, *J Alloy Compd.*, 2022, **903**, 163911.

17 A. C. García-Velasco, A. Báez-Rodríguez, M. Bizarro, R. M. Calderón-Olvera, J. Hernández-Torres, L. García-González and L. Zamora-Peredo, *J. Lumin.*, 2022, **251**, 119187.

18 A. H. Liang, R. Hu, G. R. Li, X. P. Jiang, L. Y. Zheng, Z. T. Zeng and X. S. Wang, *J. Lumin.*, 2022, **247**, 118866.

19 H. W. Xu, L. L. Wang, M. H. Li, R. Z. Houzong, Z. H. Deng, D. Qu and J. S. Shi, *Ceram. Int.*, 2017, **43**, 10967-10974.

20 B.-M. Liu, W.-J. Gan, S.-Q. Lou, R. Zou, Q. Tang, C.-X. Wang, J. Jiao and J. Wang, *J. Appl. Phys.*, 2021, **129**, 120901.

21 B. Ma, J. Ding, Q. Long and Y. Wang, *J. Lumin.*, 2019, **208**, 388-393.

22 A. Sahai and N. Goswami, *Ceram. Int.*, 2014, **40**, 14569-14578.

23 S. K. Pandey, C. Mukherjee, P. Mishra, M. Gupta, S. R. Barman, S. W. D'Souza and S. Mukherjee, *J. Mater. Sci. Mater. Electron.*, 2013, **24**, 2541-2547.

24 F. H. Bo, Y. S. Yan, Z. P. Feng, W. H. Yuan, L. X. Lin, J. C. Mei, Z. Q. Sheng, C. Y. Hai and W. Z. Guo, *Chin. Phys. Lett.*, 2007, **24**, 2108-2111.

25 S. Y. Li, Q. Zhu, J. Q. Xiahou and J.-G. Li, *Dalton Trans.*, 2022, **51**, 1112-1122.

26 J. Zhang, X. W. Li and G. B. Chen, *Mater. Chem. Phys.*, 2018, **206**, 40-47.

27 J.-G. Li, X. D. Li, X. D. Sun and T. Ikegami, *Chem. Mater.*, 2008, **20**, 2274-2281.

28 A. J. J. Bos, *Mater.*, 2017, **10**, 1357.

29 J.-M. Ducruet and I. Vass, *Photosynth. Res.*, 2009, **101**, 195-204.

30 Y.-C. Li, Y.-H. Chang, Y.-S. Chang, Y.-J. Lin and C.-H. Laing, *J. Phys. Chem. C*, 2007, **111**, 10682-10688.

31 X. J. Wang, J.-G. Li, Q. Zhu and X. D. Sun, *J. Am. Ceram. Soc.*, 2015, **98**, 3236-3242.

32 J. X. Wu, M. Li, M. T. Wang, Z. G. Liu and H. L. Jia, *J. Lumin.*, 2018, **197**, 219-227.

33 S. K. Gupta, K. Sudarshan, B. Modak, A. K. Yadav, P. Modak, S. N. Jha and D. Bhattacharyya, *J. Phys. Chem. C*, 2020, **124**, 16090-16101.

34 M. L. Moreira, E. C. Paris, G. S. do Nascimento, V. M. Longo, J. R. Sambrano, V. R. Mastelaro, M. B. Bernardi, J. Andrés, J. A. Varela and E. Longo, *Acta Mater.*, 2009, **57**, 5174-5185.

35 S. Yang and S. Park, *J. Phys. Chem. Lett.*, 2022, **13**, 9766-9770.

36 H. M. Li, R. Pang, G. Y. Liu, W. Z. Sun, D. Li, L. H. Jiang, S. Zhang, C. Y. Li, J. Feng and H. J. Zhang, *Inorg. Chem.*, 2018, **57**, 12303-12311.

37 Z. Y. Yang, S. Q. Lai and Z. G. Xia, *J. Solid State Chem.*, 2020, **288**, 121408.

38 J. C. Gong, W. Q. Luo, W. R. Lan, X. Chen and H. Y. Wu, *Spectrochim. Acta, Part A*, 2022, **266**, 120416.

39 Y. Huang, Y. M. Yu, T. Tsuboi and H. J. Seo, *Opt. Express*, 2012, **20**, 4360-4368.

40 X. Chen, Z. G. Xia, M. Yi, X. C. Wu and H. Xin, *J. Phys. Chem. Solids*, 2013, **74**, 1439-1443.

41 A. V. Dijken, J. Makkinje and A. Meijerink, *J. Lumin.*, 2001, **92**, 323-328.

42 Z. B. Pan, P. Loiko, S. Slimi, H. L. Yuan, Y. C. Wang, Y. G. Zhao, P. Camy, E. Dunina, A. Kornienko, L. Fomicheva, L. Wang, W. D. Chen, U. Griebner, V. Petrov, R. M. Solé, F. Díaz, M. Aguiló and X. Mateos, *J. Lumin.*, 2022, **246**, 118828.

43 Z. L. Chen, Z. B. Tian, J. Zhang, F. Li, S. M. Du, W. Cui, X. Y. Yuan, K. X. Chen and G. H. Liu, *J. Am. Ceram. Soc.*, 2022, **105**, 2094-2104.